



Unprecedentedly efficient mineralization performance of photocatalysis-self-Fenton system towards organic pollutants over oxygen-doped porous $\text{g-C}_3\text{N}_4$ nanosheets

Fei Wang ^{a,b,c,d}, Jing Xu ^{a,b,c,d,*}, Zhouping Wang ^{a,b,c,d,e,f}, Yang Lou ^g, Chengsi Pan ^g, Yongfa Zhu ^h

^a State Key Laboratory of Food Science and Technology, Jiangnan University, Wuxi 214122, PR China

^b School of Food Science and Technology, Jiangnan University, Wuxi 214122, PR China

^c International Joint Laboratory on Food Safety, Jiangnan University, Wuxi 214122, PR China

^d Collaborative Innovation Center of Food Safety and Quality Control in Jiangsu Province, Jiangnan University, Wuxi 214122, PR China

^e National Engineering Research Center for Functional Food, Jiangnan University, Wuxi 214122, PR China

^f Key Laboratory of Meat Processing of Sichuan, Chengdu University, Chengdu 610106, PR China

^g School of Chemical and Material Engineering, Jiangnan University, Wuxi 214122, PR China

^h Department of Chemistry, Tsinghua University, Beijing 100084, PR China



ARTICLE INFO

Keywords:

Photocatalysis-self-Fenton
 $\text{G-C}_3\text{N}_4$
 in-situ H_2O_2 generation
 Organic pollutants
 Mineralization

ABSTRACT

Herein, a photocatalysis-self-Fenton system was constructed to achieve unprecedentedly efficient degradation and mineralization performance towards organic pollutants. This system is based on oxygen-doped porous $\text{g-C}_3\text{N}_4$ nanosheets (OPCN) with high H_2O_2 yield and the added Fe^{3+} . The corresponding degradation rate for 2,4-dichlorophenol was 11.5 and 9.9 times higher than that of bulk- $\text{g-C}_3\text{N}_4$ -based photocatalysis and Fenton system, respectively, while the mineralization rate was 11.4 and 4.2 times higher, respectively. The excellent oxidation capacity was due to three reasons: (1) the porous nanosheet morphology and oxygen doping of HCNS accelerated the carriers transfer and provided more reactive sites for H_2O_2 synthesis; (2) Fe^{3+} was reduced into Fe^{2+} by photogenerated electrons, further inhibiting the charge recombination and promoting the cyclic conversion of $\text{Fe}^{3+}/\text{Fe}^{2+}$; (3) the high-efficiency utilization of in-situ generated H_2O_2 was realized via heterogeneous Fenton reaction, producing abundant $\bullet\text{OH}$. This work provides a new strategy to develop $\text{g-C}_3\text{N}_4$ -based photocatalysis-self-Fenton system for environmental remediation.

1. Introduction

In recent years, the discharge of wastewater containing phenolic compounds and antibiotics has caused serious water environmental pollution, posing a great threat to ecological safety and human health. Phenolic compounds are a kind of non-biodegradable organic pollutants, which have been commonly used as pesticides, herbicides, germicides and preservatives. Phenolic compounds can cause huge damage to organisms even at an extremely low concentration [1,2]. In addition, there are a variety of antibiotics existed in wastewater due to the widespread application in the treatment of bacterial diseases, which can adversely affect the ecological systems by inhibiting the growth of microorganisms and inducing the antibiotic resistant bacteria [3–5]. Thus, the development of deep processing technology to remove and

mineralize the phenolic compounds and antibiotics in water environment is an urgent demand in environmental protection. Nowadays, advanced oxidation processes (AOPs), such as Fenton and photocatalysis technology, have attracted increasing attention in the field of pollution remediation due to simple operation, mild reaction condition and low selectivity [6–10]. Although they have been successfully used in the treatment of industrial organic wastewater, there are still some problems. The Fenton reaction process requires external addition of H_2O_2 , resulting in high processing costs [11]; The pH range ($\text{pH} \leq 3$) of homogeneous Fenton system is narrow [12–14]; Fe^{3+} is difficult to separate and recover from wastewater after the reaction, which is easy to turn into iron sludge [15–17]; How to increase the cycle conversion rate of $\text{Fe}^{3+}/\text{Fe}^{2+}$, reduce the consumption of H_2O_2 , and expand the pH range of the reaction system are the key issues to improve the removal

* Corresponding author at: State Key Laboratory of Food Science and Technology, Jiangnan University, Wuxi 214122, PR China.

E-mail address: xujing823@jiangnan.edu.cn (J. Xu).

efficiency towards organic pollutants of Fenton oxidation process. The photocatalytic technology also has defects such as low solar energy utilization, poor charge transfer efficiency and insufficient mineralization activity [18]. How to improve the light absorption ability and accelerate the carrier separation efficiency of the photocatalyst without weakening its oxidation capacity is an important breakthrough to achieve the goal of thorough mineralization towards organic pollutants.

For this purpose, some researchers have tried to introduce the Fenton reaction into the photocatalytic system by decorating iron species on the photocatalyst and adding H_2O_2 , resulting in a photocatalysis-Fenton synergistic system with superior oxidation capacity than a single AOPs [19]. In the photocatalysis-Fenton system, photogenerated electrons can be quickly transferred to Fe^{3+} and then reduced to Fe^{2+} , thereby accelerating the charge separation and promoting the cycle conversion of $\text{Fe}^{3+}/\text{Fe}^{2+}$ [20]. Meanwhile, a large number of hydroxyl radicals ($\bullet\text{OH}$) can be generated through the reaction between Fe^{2+} and the added H_2O_2 , which greatly improves the degradation and mineralization performance towards refractory organic pollutants [21,22]. For example, Yoon et al. prepared a Fe-doped g-C₃N₄/WO₃ composite photocatalyst. With the addition of H_2O_2 , more $\bullet\text{OH}$ were produced through the reaction with the doped Fe, which significantly improved the degradation efficiency of the photocatalysis-Fenton system for nitrophenol [6]. This work fully proved that photocatalysis coupled with Fenton technology was an effective strategy to improve the removal efficiency of organic pollutants. However, H_2O_2 , the essential element of the Fenton reaction, needs to be added rather than generated by the coupling system itself, which not only increases the cost of wastewater treatment but also limits the application prospects of coupling technology. Therefore, how to realize the photocatalysis-Fenton coupling technology without adding H_2O_2 is a key factor to enhance the application potential in water treatment. Photocatalysis-self-Fenton system is one kind of photocatalysis-Fenton synergistic system based on photocatalyst with high H_2O_2 production ability and iron species. H_2O_2 in-situ generated by the photocatalyst could be consumed by Fe^{2+} via the heterogeneous Fenton reaction to produce abundant $\bullet\text{OH}$, resulting in the superior degradation and mineralization performance towards organic pollutants.

Traditional inorganic photocatalysts have limited yields for H_2O_2 production, which should be due to the low ability of photogenerated holes to oxidize H_2O , the difficulty of photogenerated electrons to carry out two-electron reduction towards O_2 , and the easy decomposition of generated H_2O_2 [23]. Thus, seeking a photocatalyst with strong H_2O_2 oxidation ability, high selectivity for O_2 two-electron reduction and low H_2O_2 self-decomposition rate is of great significance to the construction of a photocatalysis-self-Fenton synergistic system. Graphitic carbon nitride (g-C₃N₄), an organic semiconductor photocatalyst, has been widely applied in the fields of pollutant degradation [24–26], H_2O_2 production [27,28], water splitting [29] and disinfection [30] due to its high stability, low cost, visible-light response and regulable structure [31]. Meanwhile, g-C₃N₄ has a unique potential in H_2O_2 production because of its unique surface structure and suitable valence band position [32,33]. Besides, varieties of modification methods, such as morphology controlling [28,34], defect engineering [35–37], and element doping [27,38] can effectively increase the H_2O_2 yield of g-C₃N₄. Wang et al. prepared g-C₃N₄ nanosheets with high specific surface area via the oxidation effect of ClO^- and the intercalating effect of Na^+ , which promoted the charge separation efficiency, increase the adsorption capacity for O_2 and activate the adsorbed O_2 molecules, thereby enhancing the H_2O_2 production efficiency by 10 times [28]. Zhu et al. prepared an oxygen-doped g-C₃N₄ (OCN), which could accelerate the carriers transfer efficiency, strengthen the oxidation ability for H_2O_2 , boost the selectivity of two-electron reduction towards O_2 , and reduce the self-decomposition rate of H_2O_2 , thereby increasing the H_2O_2 yield under 420 nm monochromatic light by 3.5 times in comparison with bulk g-C₃N₄. Additionally, OCN showed more excellent degradation performance towards phenol and 2,4-dichlorophenol (2,4-DCP) [39].

Therefore, g-C₃N₄ based photocatalyst can be regarded as a suitable candidate for the construction of photocatalysis-self-Fenton system due to its excellent ability to in-situ synthesize H_2O_2 .

In this work, the photocatalysis-self-Fenton system was constructed based on oxygen-doped porous g-C₃N₄ nanosheets (OPCN) photocatalyst and the added Fe^{3+} . Since the added Fe^{3+} could be reduced into Fe^{2+} by the photogenerated electrons, H_2O_2 in-situ generated by OPCN would be consumed by the reduced Fe^{2+} via the heterogeneous Fenton reaction to produce abundant $\bullet\text{OH}$. Due to the synergistic effect between photocatalysis and Fenton technology, the photocatalysis-self-Fenton system exhibited significantly high-fluent degradation and high mineralization performance for organic pollutants. Meanwhile, the structure-activity relationship between the unique structure and high H_2O_2 production ability of OPCN was carefully investigated. Moreover, the reactive species involved in the photocatalysis-self-Fenton reaction and the intrinsic mechanism for the high-efficiency removal activity were unambiguously disclosed.

2. Experimental section

2.1. Preparation of OPCN photocatalyst

OPCN was synthesized by controlled pyrolysis process using urea as the precursor. 10.0 g of ground urea was transferred to a lidded crucible (50 mL) wrapped with an aluminum foil. After heated in static air at 450 °C/490 °C/520 °C/550 °C for 2 h with a ramping rate of 3 °C min⁻¹, OPCN-X samples were obtained at different calcination temperatures. Meanwhile, OPCN-Xh samples calcined for different time were prepared at 450 °C for 1 h/2 h/3 h/4 h with a heating rate of 3 °C min⁻¹. After cooled down naturally, the resulting powder was dispersed in ultrapure water, then ultrasonicated for 3 h to obtain an aqueous suspension of 1 g L⁻¹. The final products were collected after washing several times and dried in a vacuum at 60 °C. The bulk g-C₃N₄ (BCN) synthesized from melamine via polycondensation at 550 °C for 4 h was selected as the reference g-C₃N₄ sample.

2.2. Photocatalytic H_2O_2 production experiments

The photocatalytic H_2O_2 production experiments have been carried out in the multi-channel photoreaction apparatus (Beijing Pefectlight PCX50C). First, 25 mg of photocatalyst was added to 50 mL of 5 ppm 2,4-DCP solution, then the suspension was ultrasonically dispersed for 30 min, and stirred for 30 min under dark condition to achieve adsorption-desorption equilibrium. Visible light ($\lambda > 400$ nm) was provided by the Vlight multi-channel lamp panel equipped with 10 W LED lights (100 mW cm⁻²). Oxygen was continuously supplied during the reaction. During the irradiation, about 1 mL of the suspension was taken from the reaction cell at given time intervals, and then centrifuged to remove the photocatalyst particles. Subsequently, H_2O_2 was measured by using the iodometric method. Typically, a certain volume of fluorescence reagents (0.1 M potassium hydrogen phthalate and 0.4 M potassium iodide aqueous solution) were complexed with the reaction system. By measuring the absorbance at 350 nm on a UV-Vis spectrophotometer (UV-3600 Plus, Shimadzu), the H_2O_2 concentration during each reaction period was estimated. The H_2O_2 decomposition experiments were conducted in an O_2 -saturated and visible light irradiation system. 50 mg of catalyst was suspended in 50 mL of H_2O_2 aqueous solution (10 mM) in the Quartz tube. Then the system was irradiated by visible light for 2 h and measured the residual concentration of H_2O_2 .

2.3. Photocatalysis-self-Fenton degradation experiments

The degradation efficiency towards organic pollutants under visible light irradiation was evaluated in a multi-channel photoreaction apparatus (Beijing Pefectlight PCX50C). Visible light ($\lambda > 400$ nm) was provided by the Vlight multi-channel lamp panel equipped with 10 W

LED lights (100 mW cm^{-2}). First, 25 mg of photocatalyst was added to 50 mL of pollutant solution with a certain concentration (5 ppm 2,4-DCP/5 ppm phenol/5 ppm tetrachlorophenol (4-CP)/10 ppm bisphenol A (BPA)/10 ppm ofloxacin). Then the suspension was ultrasonically dispersed for 30 min and stirred for 30 min under dark condition to achieve adsorption-desorption equilibrium. 20 mg of $\text{FeCl}_3 \cdot 6\text{H}_2\text{O}$ was added to the reaction system. O_2 -pumping was kept throughout the whole reaction process. After irradiation with visible light, 2 mL of the solution was taken at regular intervals, centrifuged, and filtered with a $0.22 \mu\text{m}$ Millipore filter to remove the photocatalyst. Finally, the concentrations of organic pollutants were detected by high-performance liquid chromatography (HPLC). The liquid chromatographic conditions for different organic pollutants such as 2,4-DCP, phenol, BPA, 4-CP and ofloxacin were shown in Table S1.

3. Results and discussion

3.1. Efficient photocatalytic H_2O_2 production ability of oxygen-doped porous $\text{g-C}_3\text{N}_4$ nanosheets

As shown in Fig. S1a and Fig. S1b, among all the $\text{g-C}_3\text{N}_4$ samples synthesized at different calcination temperatures and time, the sample calcined at 450°C for 2 h (450°C –2 h) has the best photocatalytic H_2O_2 generation performance. Thus, 450°C –2 h was selected as the calcination condition of OPCN in this work. Since bulk $\text{g-C}_3\text{N}_4$ (BCN) synthesized at 550°C for 4 h with melamine as the precursor is the most commonly used reference $\text{g-C}_3\text{N}_4$ sample, we also selected BCN to compare the effects of porous nanosheet structure and oxygen doping on the photocatalytic H_2O_2 production performance of OPCN.

As observed in transmission electron microscopy (TEM) images, BCN exhibits a massive particle shape with layered structure (Fig. S2), while OPCN has a nanosheet-like structure with a large number of nanopores formed on the surface (Fig. 1a). Ammonia released during the pyrolysis of urea can etch the surface of $\text{g-C}_3\text{N}_4$, thereby resulting in the porous nanosheet morphology of OPCN. Compared with BCN, OPCN has much higher specific surface area ($53.67 \text{ m}^2 \text{ g}^{-1}$) and pore volume ($0.129 \text{ cm}^3 \text{ g}^{-1}$) (Table S2). Besides, OPCN shows type IV adsorption-desorption isotherms with a pore size range of 2–20 nm, demonstrating its mesoporous characteristics (Fig. S3) [40,41]. The porous nanosheet structure is conducive to promoting the formation of abundant active sites and the migration of photogenerated carriers from birthplace to surface, finally enhancing the catalytic performance. As shown in the X-ray diffraction (XRD) patterns (Fig. 1b), the (100) diffraction peak of OPCN is almost disappeared in comparison with BCN, which is owing to the destruction of long-range ordered structure of $\text{g-C}_3\text{N}_4$ during the thermal etching process [42]. Meanwhile, the (002) peak of OPCN is significantly shifted to a lower angle than that of BCN due to the increase of the interlayer spacing after morphological adjustment. Moreover, a new diffraction peak appeared at 10.6° of OPCN might be attributed to the introduction of oxygen-containing functional groups that affect the symmetrical structure of $\text{g-C}_3\text{N}_4$. Compared with BCN, OPCN exhibits more pronounced Fourier transform infrared spectroscopy (FTIR) absorption peak around 3400 cm^{-1} (Fig. 1c), which is due to the doping of oxygen atoms in the framework of $\text{g-C}_3\text{N}_4$ after the pyrolysis treatment, thereby forming more O-H group [43]. It is worth noting that OPCN shows a new peak at 1068 cm^{-1} corresponding to the C-O-C vibration, also indicating the successful introduction of oxygen-containing groups [44]. Notably, according to the elemental analysis results (Table S3), the content of O

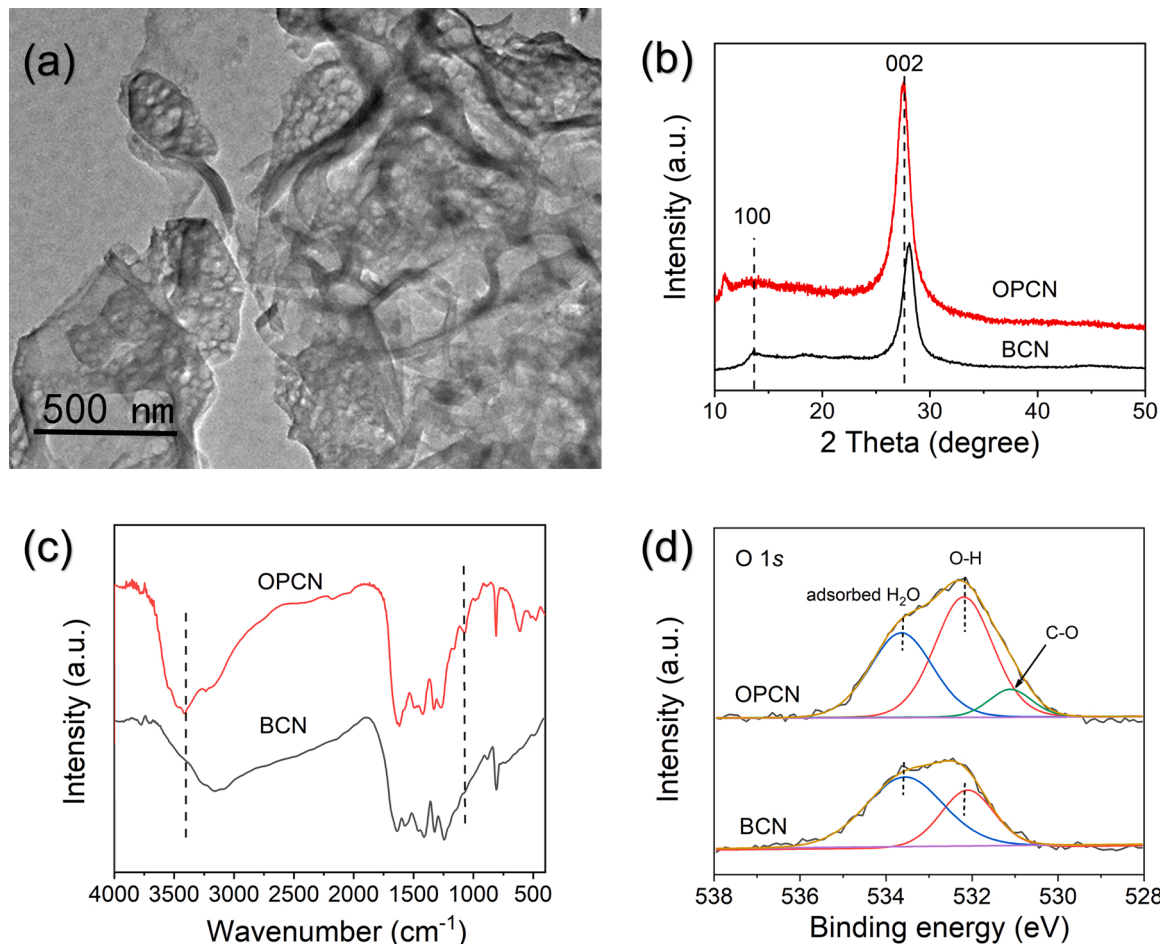


Fig. 1. (a) TEM of OPCN, (b) XRD patterns, (c) FTIR spectra and (d) high-resolution O 1s XPS spectra of BCN and OPCN.

in OPCN is significantly higher than that of BCN, which is in accordance with the FTIR results. To further certify the existence of oxygen-containing groups in OPCN, X-ray photoelectron spectroscopy (XPS) analysis was also performed (Fig. S4). The O 1s spectrum of BCN (Fig. 1d) could be fitted into two peaks at about 532.2 eV and 533.6 eV, which can be ascribed to the O-H bond and the surface adsorbed H_2O molecules, respectively. For OPCN, the intensity of the O-H peak is significantly higher than that of BCN, and a new peak corresponding to the C-O bond is centered at 531.1 eV, evidencing that the oxygen-containing groups are successfully introduced into the skeleton of $\text{g-C}_3\text{N}_4$ [45].

Based on the aforementioned research, we speculate that the porous nanosheet structure and oxygen-containing groups formed in the framework of OPCN could enable the efficient charge separation. Thus, the optical and photoelectrochemical properties of OPCN were studied to analyze the behavior of the photogenerated carriers. As revealed in UV-V is diffuse reflectance spectra (DRS) (Fig. S5a), although the absorption edge of OPCN is blue-shifted in comparison with BCN, the light-harvesting ability in the range of 200–400 nm is greatly improved. This is mainly due to the multiple reflection/scattering of incident light within the porous structure of OPCN. On the basis of the schematic band structures (Fig. S5d) calculated by Tauc-Plot method (Fig. S5b) and Mott-Schottky plots (Fig. S5c), the conduction band (CB) potential (E_{CB}) of OPCN positively shifts by 0.08 V in comparison with BCN, indicating that the electronic structure has been changed due to the oxygen doping existed in the skeleton according to the previous reports [42]. Besides, the valence band (VB) potential (E_{VB}) of OPCN (2.39 V vs. NHE) is more positive than that of BCN (2.18 V vs. NHE), indicating that the photogenerated holes of OPCN possess stronger oxidation capacity. As shown in photoluminescence (PL) spectra (Fig. S6a), the emission peak of OPCN is blue-shifted with higher intensity than that of BCN, which should be related to its porous nanosheet structure. Meanwhile, the average lifetimes of OPCN and BCN determined by time-resolved fluorescence decay spectroscopy are 9.11 ns and 7.46 ns, respectively (Fig. S6b and Table S4), indicating the lifetime of photogenerated carriers participating in the reaction has been prolonged [46]. The photocurrent response intensity of OPCN is about 2.0 times higher than that of BCN, suggesting that a larger number of photogenerated electrons could be transferred from OPCN to the ITO glass substrate (Fig. S7a) [47]. It is conducive to the photocatalytic H_2O_2 production reaction which requires abundant electrons to reduce O_2 . Additionally, OPCN shows a smaller arc radius than BCN in the electrochemical impedance spectroscopy (EIS) Nyquist plots under visible light (Fig. S7b), implying the reduced charge transfer resistance and improved charge separation efficiency [24,48]. The superior optical properties and photoelectric

conversion performance of OPCN should be ascribed to its unique structural characteristics as follows: (1) the porous nanosheet structure could optimize the light absorption ability and shorten the distance for the charge carriers to transport from birthplace to surface; (2) the oxygen doping could adjust the band structure and suppress the recombination of photogenerated electron-hole pairs.

The photocatalysis-self-Fenton system is based on the Fenton reaction between Fe^{2+} and H_2O_2 generated in-situ by the photocatalyst. The added Fe^{3+} could be reduced by the photogenerated electrons to form Fe^{2+} , which would react with H_2O_2 generated by OPCN to produce abundant $\bullet\text{OH}$ with strong oxidation capacity, thereby achieving high-efficiency degradation and mineralization performance. Thus, the removal efficiency of photocatalysis-self-Fenton system towards organic pollutants largely depends on the H_2O_2 production activity of the photocatalyst. Herein, the photocatalytic H_2O_2 generation experiments were conducted by directly using 2,4-DCP as the sacrificial agent. The H_2O_2 production activity of BCN is poor, the accumulation concentration of H_2O_2 after 2 h of visible light irradiation is only 6.37 μM . By contrast, the H_2O_2 yield of OPCN is substantially enhanced, the cumulative concentration of H_2O_2 within 2 h can reach 50.12 μM , which is about 7.9-folds higher than that of BCN (Fig. 2a). The mechanism for the remarkably improved photocatalytic H_2O_2 generation activity of OPCN can be explained by two factors: (1) the well-developed porosity of OPCN with high surface area could provide larger amount of 1,4-endoperoxide species on the surface which would effectively promote the two-electron reduction towards O_2 , resulting in high selectivity of H_2O_2 generation [49]; (2) the introduced oxygen-containing groups in the framework could not only strengthen the oxidation ability for H_2O , but also make the formation of 1,4-endoperoxide species much easier [39]. Besides, the stability of H_2O_2 generation over OPCN was evaluated by the recycle test and light-driven H_2O_2 decomposition test. After 4 cycles, the photocatalytic activity of OPCN has no apparent decrease with isopropanol as a sacrificial agent, which proves that it has excellent stability (Fig. 2b). In addition, the H_2O_2 decomposition ratio after 2 h of irradiation over OPCN (2.4%) is smaller than BCN (6.4%), demonstrating that OPCN possesses a low self-decomposition rate of H_2O_2 (Fig. S8).

In summary, the porous nanosheet morphology and the introduced oxygen-containing groups in the framework of OPCN could accelerate the separation efficiency of photogenerated carriers, strengthen the oxidation ability for H_2O , boost the selectivity of two-electron reduction towards O_2 , and reduce the self-decomposition rate of H_2O_2 , finally resulting in the greatly enhanced photocatalytic H_2O_2 production activity.

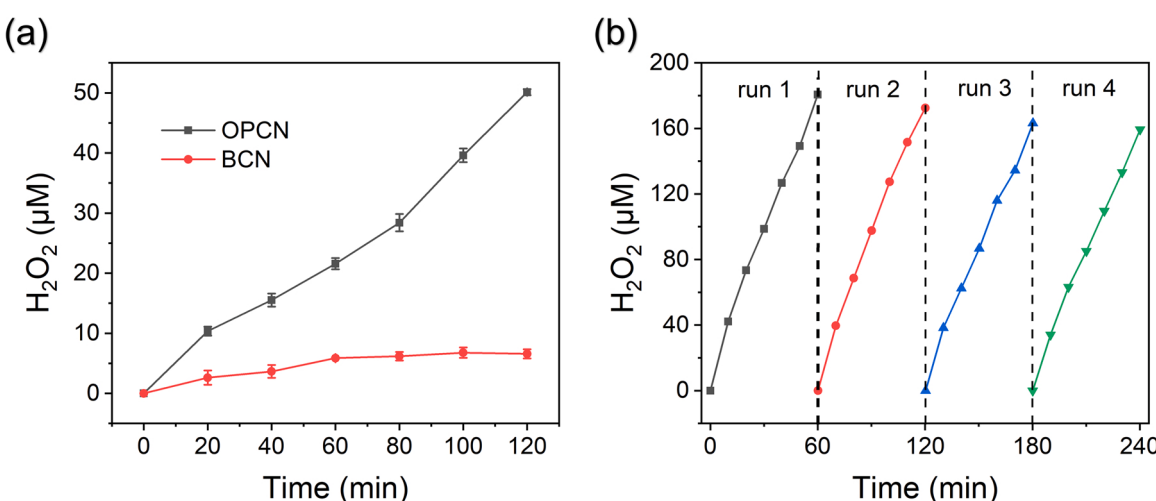


Fig. 2. (a) The photocatalytic H_2O_2 generation curves of BCN and OPCN. (b) The recycle test of H_2O_2 generation of OPCN.

3.2. Construction of the photocatalysis-self-Fenton system based on OPCN

The scheme of the photocatalysis-self-Fenton system for pollutant degradation based on OPCN is proposed and shown in Fig. 3. Under visible light irradiation, the 1,4-endoperoxide formed on the surface of OPCN promotes the two-electron reduction towards O_2 , resulting in the highly selective production of H_2O_2 . Meanwhile, Fe^{3+} is reduced to Fe^{2+} by photogenerated electrons and then reacts with H_2O_2 to generate a large number of $\bullet OH$ to attack organic pollutants and degrade them into small molecules such as H_2O and CO_2 . Hence, the photocatalysis-self-Fenton system is constructed to realize the synergistic effect between photocatalysis and Fenton reaction.

The optimal conditions for photocatalysis-self-Fenton degradation, such as the pH value, the iron species type and the usage amount of ferric salt, were systematically explored to achieve the best removal efficiency towards organic pollutants. As shown in Fig. S9a, when the pH value is controlled as 4.5, 6.0 and 7.5, the 2,4-DCP degradation rate constant (k) of OPCN within 1 h under visible light is 0.022 min^{-1} , 0.010 min^{-1} and 0.014 min^{-1} , respectively. Although the removal ratio is highest at pH = 4.5, ferric salt is easily turned into iron sludge under weak acidic condition. Thus, the pristine pH value without adjustment was selected to carry out the photocatalysis-self-Fenton degradation experiment to highlight its universality applied in different pH conditions. The influence of different iron species ($FeSO_4$ and $FeCl_3$) was also compared. After 1 h of visible light irradiation, the determined k of OPCN+Fe(III) group (0.028 min^{-1}) is 2.0 times higher than that of OPCN+Fe(II) group (0.014 min^{-1}) (Fig. S9b). This is due to the fact that part of photogenerated electrons could be consumed for the reduction of Fe^{3+} to produce Fe^{2+} , thus promoting the charge separation and improving the degradation activity. Hence, $FeCl_3$ was chosen as the iron species added to the system. Besides, the usage amount of $FeCl_3$ was optimized. When the amount of $FeCl_3$ increases from 5.0 mg to 20.0 mg, the degradation activity gradually increases. The determined k of 20.0 mg group (0.069 min^{-1}) is about 5.3 times as that of 5.0 mg group (0.013 min^{-1}) (Fig. S9c), which might be related to the improvement of H_2O_2 utilization efficiency. However, the degradation activity reduces when the usage of $FeCl_3$ increases to 25.0 mg due to the decreased light transmittance. Thus, the addition amount of $FeCl_3$ in the system was selected as 20 mg. To sum up, the optimal conditions for the photocatalysis-self-Fenton degradation system were determined as follows: the pH value was pristine without adjustment, $FeCl_3$ was utilized as the iron species, and the usage amount of $FeCl_3$ was 20.0 mg.

Moreover, the impact of the added Fe^{3+} on the photon absorption of the photocatalysis-self-Fenton system was investigated by measuring the photon absorption intensity, the specific extinction coefficient and the

optical thickness in the reactor of OPCN photocatalyst with and without Fe^{3+} according to the evaluation methods reported by other works [50–52]. As shown in Fig. S10a, it is found that the UV-Vis absorption spectrum of $FeCl_3$ has not overlapped with the UV-Vis DRS of OPCN photocatalyst in the visible region ($\lambda > 400\text{ nm}$), suggesting that the presence of Fe^{3+} should not affect the absorption of OPCN photocatalyst in the visible region. As shown in Fig. S10b, the photon absorption intensities for OPCN and OPCN+Fe(III) suspensions in the reactor are measured to be 91.37 mW cm^{-2} and 94.10 mW cm^{-2} , respectively. As shown in Fig. S10c, the specific extinction coefficients of OPCN and OPCN+Fe(III) suspensions are determined as a function of wavelength in the visible region from 400 nm to 440 nm, and OPCN+Fe(III) shows slightly higher values than OPCN. The estimated spectral-averaged specific extinction coefficients of OPCN and OPCN+Fe(III) suspensions are $399.6\text{ m}^2\text{ kg}^{-1}$ and $432.7\text{ m}^2\text{ kg}^{-1}$, respectively, while the optical thicknesses of OPCN and OPCN+Fe(III) suspensions in the reactor are calculated to be 13.6 and 14.7, respectively. To sum up, compared with OPCN, the photon absorption intensity, the specific extinction coefficient and the optical thickness in the reactor of OPCN+Fe(III) only increase slightly, indicating that the added Fe^{3+} has a relatively small impact on the photon absorption of the photocatalysis-self-Fenton system in the visible region.

3.3. The degradation and mineralization performance of photocatalysis-self-Fenton system based on OPCN

As shown in Fig. 4a, the 2,4-DCP degradation activities of BCN and OPCN are not satisfactory in the photocatalysis system, while the removal rates of both catalysts increase greatly in the photocatalysis-self-Fenton system. Surprisingly, the k value of OPCN-based photocatalysis-self-Fenton system even rises to 0.069 min^{-1} , which is 9.9 times as that of its own photocatalysis system (0.007 min^{-1}), 9.9 times as that of BCN-based photocatalysis-self-Fenton system (0.007 min^{-1}), and 11.5 times as that of BCN-based photocatalysis system (0.006 min^{-1}) (Fig. 4b). In addition, total organic carbon (TOC) analysis is an important indicator for evaluating the mineralization ability of organic pollutant removal technology. Fig. 4c clearly shows that the TOC removal rate of the photocatalysis-self-Fenton system is significantly higher than that of photocatalysis system. After 2 h of 2,4-DCP degradation reaction, the TOC removal rate of the OPCN-based photocatalysis-self-Fenton system is 42.22%, which is 5.6 times as that of its own photocatalysis system (7.49%), 6.0 times as that of BCN-based photocatalysis-self-Fenton system (7.01%), and even nearly 11.4 times as that of BCN-based photocatalysis system (3.69%). The TOC removal rate of OPCN-based photocatalysis-self-Fenton system enhances with the

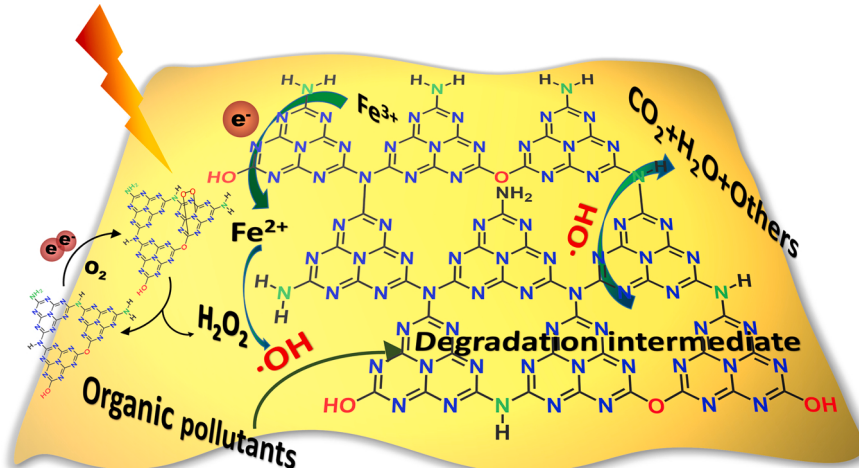


Fig. 3. Schematic illustration of the photocatalysis-self-Fenton system based on OPCN.

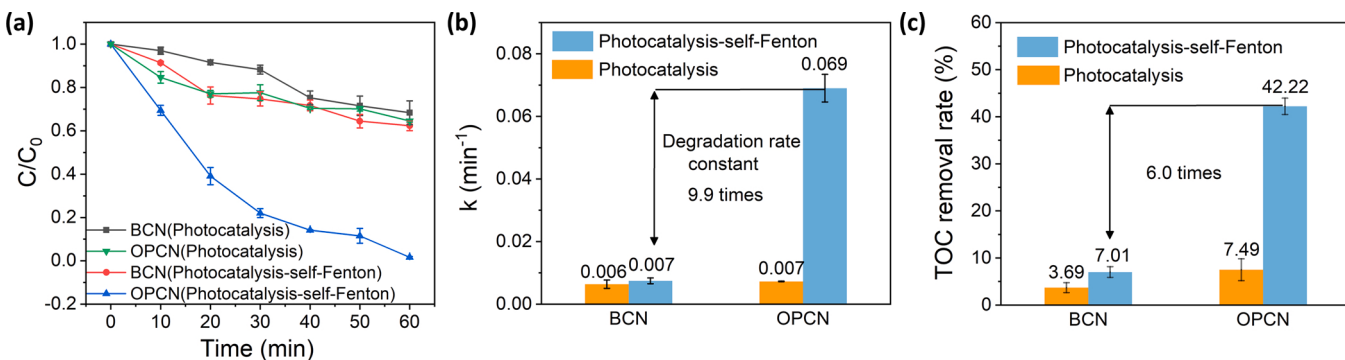


Fig. 4. The comparison of (a) the 2,4-DCP degradation activity, (b) the degradation rate constant and (c) TOC removal rate between photocatalysis-self-Fenton and photocatalysis based on OPCN and BCN.

increase of the corresponding degradation rate, indicating that the degradation and mineralization occur simultaneously in the organic pollutant removal process. Compared with photocatalysis, the superior degradation and mineralization performance of the photocatalysis-self-Fenton system are attributed to the highly efficient utilization of H_2O_2 in-situ generated by OPCN and consumption in the Fenton reaction, which can efficiently produce more $\bullet\text{OH}$ with strong oxidizing ability to degrade organic pollutants, and then mineralize the pollutants into small molecular substances.

Meanwhile, the degradation and mineralization performance of photocatalysis-self-Fenton and Fenton technology were further compared. The amount of external addition of H_2O_2 in the Fenton reaction was designed as 13.3, 26.5 and 53.0 μM , which was 0.5, 1.0 and 2.0 times as the cumulative concentration of H_2O_2 generated by OPCN-based photocatalysis within 60 min of visible light irradiation with 2,4-DCP as the sacrificial agent, respectively. Interestingly, after H_2O_2 is added to the Fenton system, the 2,4-DCP degradation rate quickly reaches the maximum in a short time and levels off with the extension of time. As the addition amount of H_2O_2 in the Fenton system increases from 13.3 μM to 53.0 μM , the degradation efficiency also raises from 18.09% to 55.26%, which is much lower than that of photocatalysis-self-Fenton system (98.37%) (Fig. 5a). By contrast, the k value of photocatalysis-self-Fenton system (0.069 min^{-1}) is about 9.9 times that of the Fenton system with the addition of 26.5 μM of H_2O_2 (0.007 min^{-1}) (Fig. 5b). For Fenton technology, the externally added H_2O_2 could not react with Fe^{2+} in time, resulting in the low utilization efficiency and self-decomposition of H_2O_2 [53]. In contrast, although the amount of in-situ generated H_2O_2 is relatively low in the photocatalysis-self-Fenton system, the efficient utilization of H_2O_2 promotes the sustainable production of $\bullet\text{OH}$, further improving its degradation ability towards pollutants. Meanwhile, it can be seen in Fig. 5c that the TOC removal rate of the photocatalysis-self-Fenton system reaches 42.22%, which is nearly 4.2 times as that of the Fenton system

with 26.5 μM of H_2O_2 (10.09%). Therefore, the photocatalysis-self-Fenton system also exhibits more excellent degradation and mineralization performance in comparison with the Fenton system.

Excitingly, the photocatalysis-self-Fenton system based on OPCN also exhibits highly efficient degradation and mineralization performance for other phenolic pollutants and antibiotic pollutants. As shown in Fig. 6a, the degrading efficiencies of phenol, BPA, 4-CP and ofloxacin over the photocatalysis-self-Fenton system are 3.4, 2.9, 2.2 and 1.5 times higher than those of photocatalysis system, respectively. Meanwhile, the TOC removal rates of phenol, BPA, 4-CP and ofloxacin over the photocatalysis-self-Fenton system are 1.8, 2.9, 4.8 and 3.4 times as those of the photocatalytic system, respectively (Fig. 6b). The above results illustrate the wide applicability for the removal of various organic pollutants over the photocatalysis-self-Fenton system.

Moreover, to further evaluate the stability and reusability of the photocatalysis-self-Fenton system based on OPCN, the recycling tests were performed for 2,4-DCP degradation. As shown in Fig. S11a, there is a slight decrease in activity after 4 cycles of consecutive degradation, which might be due to the loss of catalyst during the separation process. Meanwhile, after 4 cycles, the XRD pattern and FTIR spectrum of the used OPCN are almost similar to the initial results, further proving that OPCN photocatalyst has high stable structure (Fig. S11b and S11c).

3.4. Mechanism of the photocatalysis-self-Fenton system based on OPCN

To clarify the reaction mechanism of the photocatalysis-self-Fenton system for the high-efficiency degradation and mineralization performance towards organic pollutants, atmosphere control experiments, radical trapping tests and electron spin resonance (ESR) analysis were carried out. As shown in Fig. 7a, the k value of OPCN under O_2 atmosphere (0.008 min^{-1}) is negligible, which is due to the limited oxidation capacity of photocatalysis system [54]. By contrast, the k value of OPCN

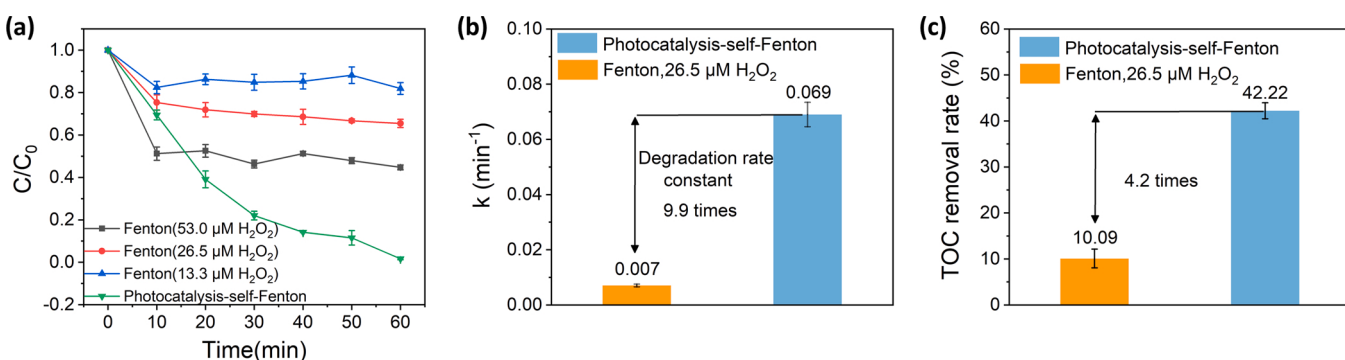


Fig. 5. The comparison of (a) the 2,4-DCP degradation activity, (b) the degradation rate constant and (c) TOC removal rate between Fenton and photocatalysis-self-Fenton based on OPCN.

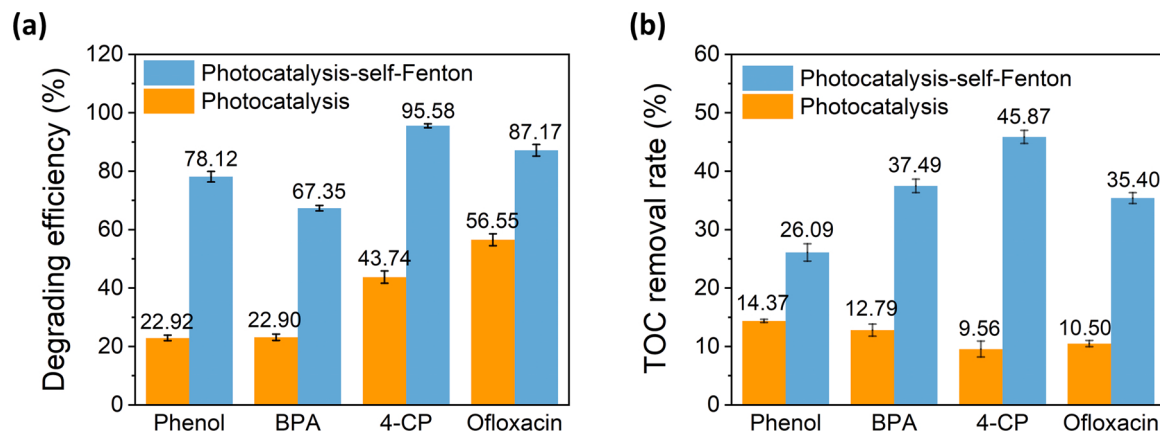


Fig. 6. The comparison of (a) the degrading efficiency and (b) TOC removal rate between photocatalysis-self-Fenton and photocatalysis based on OPCN towards various organic pollutants.

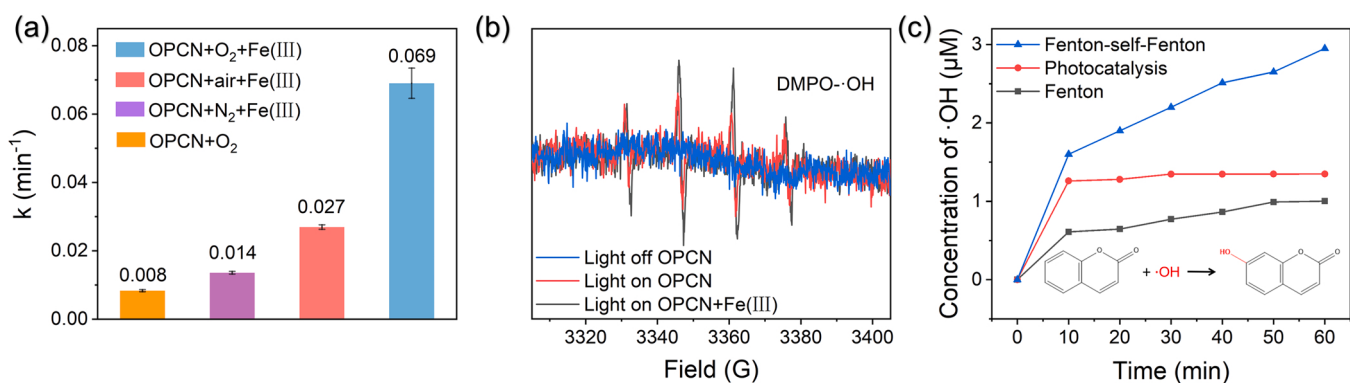


Fig. 7. (a) The comparison of the 2,4-DCP degradation rate constants of the photocatalysis-self-Fenton system based on OPCN under different control conditions. (b) ESR analysis of OPCN under dark and visible light for the detection •OH. (c) The concentration changes of •OH in photocatalysis, Fenton and photocatalysis-self-Fenton system.

under N₂ atmosphere (0.014 min⁻¹) is improved with the addition of Fe³⁺, but it is much lower than that under air atmosphere (0.027 min⁻¹), indicating that H₂O₂ can only be produced via reducing O₂ by photogenerated electrons instead of directly oxidizing H₂O by photogenerated holes. Among all control groups, the photocatalysis-self-Fenton system under O₂ atmosphere has the highest k value (0.069 min⁻¹) due to the continuous pumping of O₂ throughout the reaction. Under such condition, a larger number of •OH can be produced via the Fenton reaction, while the charge separation efficiency can be accelerated through adsorbing electrons by O₂, resulting in the highly effective degradation performance.

To study the effect of reactive species on the removal efficiency of the photocatalysis-self-Fenton system based on OPCN, isopropyl alcohol (IPA) and formic acid (FA) were added to capture •OH and holes (h⁺), respectively (Fig. S12a). The 2,4-DCP degradation activity of the photocatalysis-self-Fenton system has been inhibited to varying degrees after adding different scavengers, proving that •OH and h⁺ both are the reactive species participating in the reaction. And it is easily observed that the addition of IPA significantly restrains the degradation of 2,4-DCP, indicating that •OH has a dominant influence on the degradation reaction. In ESR analysis, 5,5-dimethyl-1-pyrroline-N-oxide (DMPO) was used as a spin probe for detection of •OH and •O₂⁻, and the signals of DMPO-•OH and DMPO-•O₂⁻ were detected in H₂O and methanol, respectively. As shown in Fig. 7b, no signal is generated over OPCN under dark condition, while a weak 1:2:2:1 quartet signal can be found under visible light, suggesting that a certain number of •OH can be produced via the photocatalysis process. In comparison, the signal of •OH is noticeably enhanced after the addition of Fe³⁺, confirming that

more •OH have been produced in the photocatalysis-self-Fenton system. Meanwhile, OPCN exhibits a characteristic signal of •O₂ under visible light in methanol, and the signal intensity becomes stronger after adding Fe³⁺ (Fig. S12b), indicating that photocatalysis-self-Fenton system can generate a larger number of electrons (e⁻) to react with O₂ for more production of •O₂⁻. The above results suggest that •OH, •O₂⁻ and h⁺ are the main reactive species participating in the photocatalysis-self-Fenton reaction.

Moreover, the concentrations of •OH generated in different systems with prolonged reaction time were compared via measuring the PL signal intensity of 7-hydroxycoumarin produced by the reaction between •OH and coumarin (Fig. S13c and Fig. S13). The photocatalysis system reaches a maximum concentration of •OH (1.34 μM) within 30 min and almost stops the production over time. Analogously, the Fenton system can rapidly generate •OH within 10 min and slow down the production with time, the maximum concentration of •OH reaches 1.00 μM after 50 min of reaction. In comparison, •OH could be continuously produced in the photocatalysis-self-Fenton system, and reach the maximum value of 2.95 μM within 60 min, which is almost 2.2 and 3.0 times as that of the photocatalysis and Fenton process. Evidently, the above results indicate that the high degradation capacity and strong mineralization ability of photocatalysis-self-Fenton system are mainly attributed to the efficient generation of •OH.

In terms of the experimental results above, the mechanism of the photocatalysis-self-Fenton system based on OPCN for the removal of organic pollutants was proposed. As illustrated in Fig. 8, under visible light irradiation, OPCN was excited to generate a large number of h⁺ and e⁻. On one hand, the h⁺ on the VB can oxidize OH⁻ to generate •OH, and

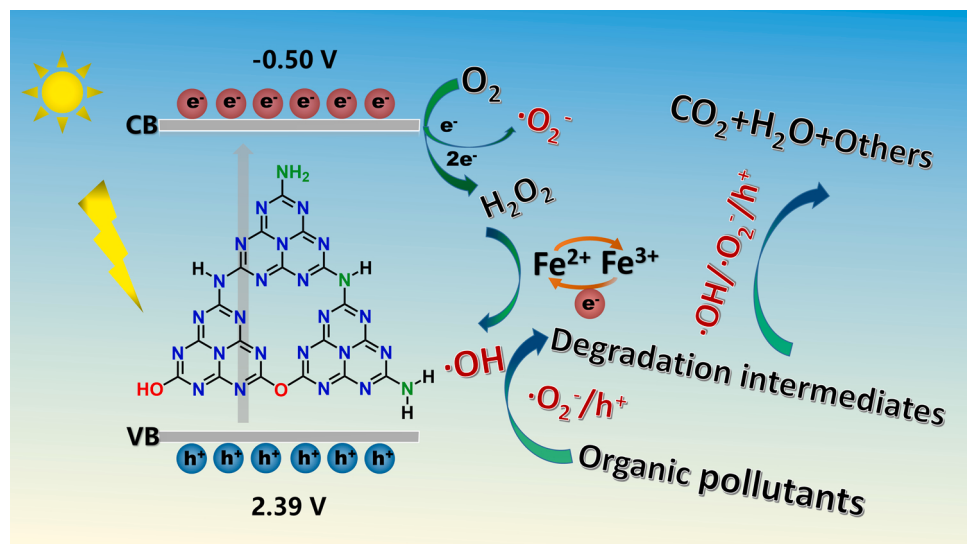


Fig. 8. The schematic diagram of proposed mechanism for the photocatalysis-self-Fenton system based on OPCN.

the e^- on the CB could reduce the adsorbed O_2 to generate $\bullet O_2^-$. On the other hand, the porous nanosheet morphology and the oxygen-containing groups introduced in the framework of OPCN could accelerate the carriers transfer efficiency, strengthen the oxidation ability for H_2O , boost the selectivity of two-electron reduction towards O_2 , and reduce the self-decomposition rate of H_2O_2 , thereby resulting in the high yield of H_2O_2 under visible light. Meanwhile, part of the e^- could reduce Fe^{3+} into Fe^{2+} , thereby further inhibiting the recombination of photo-generated e^-h^+ pairs and promoting the cyclic conversion of Fe^{3+}/Fe^{2+} . Then the in-situ generated H_2O_2 could react with Fe^{2+} to produce a large number of $\bullet OH$, which greatly enhance the oxidation capacity of the entire reaction system. Under the combined action of $\bullet OH$, $\bullet O_2^-$ and h^+ , the photocatalysis-self-Fenton system based on OPCN exhibits highly efficient degradation and mineralization performance towards organic pollutants.

4. Conclusion

In summary, a photocatalysis-self-Fenton system was constructed based on oxygen-doped porous g - C_3N_4 nanosheets (OPCN) with high H_2O_2 production ability and the addition of Fe^{3+} . The porous nanosheet morphology and the introduced oxygen-containing groups in the framework of OPCN could accelerate the carriers transfer and provide more reactive sites for H_2O_2 synthesis. The added Fe^{3+} could be reduced into Fe^{2+} by photogenerated electrons, further inhibiting the charge recombination and promoting the cyclic conversion of Fe^{3+}/Fe^{2+} . The high-efficiency utilization of in-situ generated H_2O_2 could be realized via the heterogeneous Fenton reaction, resulting in the production of abundant $\bullet OH$. Therefore, the photocatalysis-self-Fenton system based on OPCN exhibits unprecedentedly efficient degradation and mineralization performance towards organic pollutants. This work not only provides a new strategy to develop g - C_3N_4 -based photocatalyst with high H_2O_2 production activity, but also expands the application potential of photocatalysis-self-Fenton system in the field of environmental remediation.

CRediT authorship contribution statement

Fei Wang: Methodology, Validation, Formal analysis, Investigation, Data curation, Writing – original draft, Visualization. **Jing Xu:** Conceptualization, Methodology, Validation, Investigation, Resources, Writing – review & editing, Visualization, Supervision, Project administration, Funding acquisition. **Zhouping Wang:** Resources,

Supervision, Funding acquisition. **Yang Lou:** Resources. **Chengsi Pan:** Resources, Writing – review & editing. **Yongfa Zhu:** Conceptualization, Resources.

Declaration of Competing Interest

The authors declare that they have no known competing financial interests or personal relationships that could have appeared to influence the work reported in this paper.

Acknowledgements

This work was supported by the Jiangsu Agriculture Science and Technology Innovation Fund (CX(20)3108), National Natural Science Foundation of China (21707052, 31871881, 21908079 and 22172065), Fundamental Research Funds for the Central Universities (JUSRP11905) and Natural Science Foundation of Jiangsu Province (BK20211239 and BK20201345).

Appendix A. Supporting information

Supplementary data associated with this article can be found in the online version at doi:10.1016/j.apcatb.2022.121438.

References

- [1] J. Yu, T. Wang, S. Rtimi, *Appl. Catal. B Environ.* 254 (2019) 66–75.
- [2] E. Mousali, M.A. Zanjanchi, *React. Kinet. Mech. Cat.* 130 (2020) 547–566.
- [3] W. Yan, L. Yan, C. Jing, *Appl. Catal. B Environ.* 244 (2019) 475–485.
- [4] P. Chen, L. Blaney, G. Cagnetta, J. Huang, B. Wang, Y. Wang, S. Deng, G. Yu, *Environ. Sci. Technol.* 53 (2019) 1564–1575.
- [5] W. Zhang, Z. Bian, X. Xin, L. Wang, X. Geng, H. Wang, *Chemosphere* 262 (2021), 127955.
- [6] M. Yoon, Y. Oh, S. Hong, J.S. Lee, R. Boppella, S.H. Kim, F. Marques Mota, S. O. Kim, D.H. Kim, *Appl. Catal. B Environ.* 206 (2017) 263–270.
- [7] R. Saleh, A. Taufik, *Sep. Purif. Technol.* 210 (2019) 563–573.
- [8] J.J. Pignatello, E. Oliveros, A. MacKay, *Crit. Rev. Environ. Sci. Technol.* 36 (2006) 1–84.
- [9] X.N. Li, Z.M. Ao, J.Y. Liu, H.Q. Sun, A.I. Rykov, J.H. Wang, *A.C.S. Nano* 10 (2016) 11532–11540.
- [10] J. Xu, Q.Z. Gao, Z.P. Wang, Y. Zhu, *Appl. Catal. B Environ.* 291 (2021), 120059.
- [11] J. Zhang, G. Zhang, Q. Ji, H. Lan, J. Qu, H. Liu, *Appl. Catal. B Environ.* 266 (2020), 118665.
- [12] X.P. Wu, Z.D. Nan, *Mater. Chem. Phys.* 227 (2019) 302–312.
- [13] A.L. Zhang, L.Y. Zhu, Z.D. Nan, *Mater. Chem. Phys.* 224 (2019) 156–168.
- [14] X. Wang, Z. Nan, *Sep. Purif. Technol.* 233 (2020), 116023.
- [15] T. Zhou, X.H. Wu, J. Mao, Y.R. Zhang, T.T. Lim, *Appl. Catal. B Environ.* 160 (2014) 325–334.

[16] J. Zhao, M. Ji, J. Di, Y. Zhang, M. He, H. Li, J. Xia, *Photoch. Photobio. A* 391 (2020), 112343.

[17] S. Huo, W. Gao, P. Zhou, Z. Deng, Z. Han, X. Cui, X. Lu, *Adv. Powder Mater.* 1 (2022), 100028.

[18] G.L. Di, Z.L. Zhu, H. Zhang, J.Y. Zhu, Y.L. Qiu, D.Q. Yin, S. Kuppers, *J. Colloid Interf. Sci.* 538 (2019) 256–266.

[19] J. Hu, P. Zhang, W. An, L. Liu, Y. Liang, W. Cui, *Appl. Catal. B Environ.* 245 (2019) 130–142.

[20] R. Gonzalez-Olmos, M.J. Martin, A. Georgi, F.D. Kopinke, I. Oller, S. Malato, *Appl. Catal. B Environ.* 125 (2012) 51–58.

[21] C.A. Gorski, R. Edwards, M. Sander, T.B. Hofstetter, S.M. Stewart, *Environ. Sci. Technol.* 50 (2016) 8538–8547.

[22] Y. Chai, Q. Liu, L. Zhang, J. Ren, W.-L. Dai, *Chin. J. Chem.* 35 (2017) 173–182.

[23] G.-h Moon, M. Fujitsuka, S. Kim, T. Majima, X. Wang, W. Choi, *A.C.S. Catal* 7 (2017) 2886–2895.

[24] J. Xu, Z. Wang, Y. Zhu, *ACS Appl. Mater. Inter.* 9 (2017) 27727–27735.

[25] W. Ali, X. Zhang, X. Zhang, S. Ali, L. Zhao, S. Shaheen, L. Jing, *Mater. Res. Bull.* 122 (2020), 110676.

[26] J. Xu, J. Huang, Z. Wang, Y. Zhu, *Chin. J. Catal.* 41 (2020) 474–484.

[27] J. Tian, T. Wu, D. Wang, Y. Pei, M. Qiao, B. Zong, *Catal. Today* 330 (2019) 171–178.

[28] H. Wang, L. Fang, S. Hu, Y. Pei, W. Ma, *N. J. Chem.* 42 (2018) 18335–18341.

[29] A. Speltini, A. Scalabrini, F. Maraschi, M. Sturini, A. Pisani, L. Malavasi, A. Profumo, *Int. J. Hydrog. Energy* 43 (2018) 14925–14933.

[30] D. Yan, X. Wu, J. Pei, C. Wu, X. Wang, H. Zhao, *Ceram. Int.* 46 (2020) 696–702.

[31] M. Majdoub, Z. Anfar, A. Amedious, *ACS Nano* 14 (2020) 12390–12469.

[32] Y. Shiraishi, S. Kanazawa, Y. Sugano, D. Tsukamoto, H. Sakamoto, S. Ichikawa, T. Hirai, *A.C.S. Catal* 4 (2014) 774–780.

[33] Y. Kofuji, Y. Isobe, Y. Shiraishi, H. Sakamoto, S. Tanaka, S. Ichikawa, T. Hirai, *J. J. Am. Chem. Soc.* 138 (2016) 10019–10025.

[34] L. Zhou, J. Feng, B. Qiu, Y. Zhou, J. Lei, M. Xing, L. Wang, Y. Zhou, Y. Liu, J. Zhang, *Appl. Catal. B Environ.* 267 (2020), 118396.

[35] Z. Haider, H.I. Cho, G.H. Moon, H.I. Kim, *Catal. Today* 335 (2019) 55–64.

[36] S. Li, G. Dong, R. Hailili, L. Yang, Y. Li, F. Wang, Y. Zeng, C. Wang, *Appl. Catal. B Environ.* 190 (2016) 26–35.

[37] J. Xu, Z. Wang, Y. Zhu, *J. Mater. Sci. Technol.* 49 (2020) 133–143.

[38] S. Kim, G.-h Moon, H. Kim, Y. Mun, P. Zhang, J. Lee, W. Choi, *J. Catal.* 357 (2018) 51–58.

[39] Z. Wei, M. Liu, Z. Zhang, W. Yao, H. Tan, Y. Zhu, *Energ. Environ. Sci.* 11 (2018) 2581–2589.

[40] Z. Zhang, Y.J. Zhang, L.H. Lu, Y.J. Si, S. Zhang, Y. Chen, K. Dai, P. Duan, L. M. Duan, J.H. Liu, *Appl. Surf. Sci.* 391 (2017) 369–375.

[41] F. Dong, Y. Li, W. Ho, H. Zhang, M. Fu, Z. Wu, *Chin. Sci. Bull.* 59 (2014) 688–698.

[42] X. Liang, G. Wang, X. Dong, G. Wang, H. Ma, X. Zhang, *ACS Appl. Nano Mater.* 2 (2018) 517–524.

[43] M. Shen, L. Zhang, M. Wang, J. Tian, X. Jin, L. Guo, L. Wang, J. Shi, *Mater. Chem. A* 7 (2019) 1556–1563.

[44] X. Sh, J. Wu, J. Zhong, H. Xu, Y. Yang, R. Vajtai, J. Lou, Y. Liu, D. Du, H. Li, P. M. Ajayan, *Nano Energy* 27 (2016) 138–146.

[45] F. Farzin, M.K. Rofouei, M. Mousavi, J.B. Ghasemi, *J. Phys. Chem. Solids* (2022), 110588.

[46] J. Li, W. Ma, J. Chen, N. An, Y. Zhao, D. Wang, Z. Mao, *Int. J. Hydrog. Energy* 45 (2020) 13939–13946.

[47] S. Cao, B. Fan, Y. Feng, H. Chen, F. Jiang, X. Wang, *Chem. Eng. J.* 353 (2018) 147–156.

[48] Y.J. Wang, R. Shi, J. Lin, Y.F. Zhu, *Appl. Catal. B Environ.* 100 (2010) 179–183.

[49] Y. Shiraishi, Y. Kofuji, H. Sakamoto, S. Tanaka, S. Ichikawa, T. Hirai, *A.C.S. Catal* 5 (2015) 3058–3066.

[50] R. Acosta-Herazo, M.Á. Mueses, G.L. Puma, F. Machuca-Martínez, *Chem. Eng. J.* 356 (2019) 839–849.

[51] I. Grčić, G. Li Puma, *Appl. Catal. B Environ.* 211 (2017) 222–234.

[52] D. Dolat, N. Quici, E. Kusiak-Nejman, A.W. Morawski, G.L. Puma, *Appl. Catal. B Environ.* 115 (2012) 81–89.

[53] Q. Gao, J. Xu, Z. Wang, Y. Zhu, *Appl. Catal. B Environ.* 271 (2020), 118933.

[54] M. Chu, K. Hu, J. Wang, Y. Liu, S. Ali, C. Qin, L. Jing, *Appl. Catal. B Environ.* 243 (2019) 57–65.